RSC Advances

PAPER

View Article Online
View Journal | View Issue

Cite this: *RSC Adv.*, 2025, **15**, 12020

Continuous synthesis of PEGylated MIL-101(Cr) nanoparticles for neuroprotection†

Yuheng Wang[a] and Shuirong Li *[bc]

The application of metal organic frameworks (MOFs) in targeted drug delivery for ischemic stroke therapy has emerged as a hot issue recently. Although significant progress has been made in immobilizing neuroprotective agents on MOFs, environmentally friendly large-scale preparation of nano-drug-loaded MOFs with controlled size, morphology, purity and therapeutic effect remains challenging. PEGylation of MIL-101(Cr) nanoparticles with dual ligands that have the 2,2-dimethylthiazolidine (DMTD) structure was developed in this work to mitigate nervous system injury induced by ischemia/reperfusion (IR) during a stroke. A green ultrasound-assisted continuous-flow system was established for efficient production of the versatile MOF nanoparticles. Unified nanoparticles (diameter: ~250–350 nm) were obtained with both high quality and high space-time yield (5664 kg m^{-3} d^{-1}). The MOF exhibited protective activity in SH-SY5Y cells against oxygen and glucose deprivation and H_2O_2 insults, and prevented reactive oxygen species accumulation. The cellular uptake of the PEGylated MOFs by brain capillary endothelial cells was investigated, showing targeting capability *in vitro*, which proposes the biomaterial as a promising therapeutic candidate for reducing IR-induced nervous system injury.

Received 31st December 2024
Accepted 5th April 2025

DOI: 10.1039/d4ra09107h

rsc.li/rsc-advances

Introduction

The development of a controllable drug delivery system is essential for minimizing side effects and enhancing drug efficacy.[1–3] With the rapid advancement of science and technology, a novel class of porous materials known as metal–organic frameworks (MOFs) has garnered significant attention.[4–6] A MOF is a crystalline material where organic ligands act as linkers, coordinating with metal ions or clusters to create extended structures that can be one-, two-, or three-dimensional depending on the arrangement of the components within the network. Because of their unique physical and chemical properties, MOFs have been extensively studied for applications in gas storage, catalysis, molecular separation, optoelectronic devices, and sustained drug release.[7–9]

In the field of drug delivery, MOFs have a high drug-loading capacity owing to their porous structure and large specific surface area.[10,11] Additionally, the pore size and structure of MOFs can be precisely regulated by adjusting the combination of metal ions and organic ligands to facilitate controlled drug release. This adaptability affords MOFs a promising future in drug delivery applications.[12] Furthermore, MOFs have demonstrated excellent chemical stability and adaptability to various acidic, basic, and redox conditions, ensuring structural integrity and consistent drug release during delivery.[13] Their biocompatibility reduces the toxic side effects of drugs in the human body, thereby enhancing their efficacy. To date, researchers have successfully utilized MOFs to achieve the precisely controlled release of anticancer drugs, antibiotics, and gene therapy agents.[14] Moreover, the application of MOFs in biological imaging, targeted drug delivery, and controlled-release systems paves the way for innovative approaches for disease diagnosis and treatment.[15–17]

Current drug-loading strategies for MOFs primarily involve physical adsorption and chemical grafting.[18,19] Physical adsorption leverages the unique pore structure of MOFs to encapsulate drugs within these cavities. However, unlike other MOF applications, drug delivery mandates consideration of the complex microenvironment of the human body. Although physical adsorption is the most widely reported MOF strategy for drug delivery, it has certain limitations. Alternatively, chemical grafting involves modifying MOFs by attaching active components to their post-construction surfaces. Although this method results in more stable drug attachment, it restricts the active components to the MOF surface, thereby affecting the overall drug-loading capacity.

In addition to physical adsorption and chemical grafting, another effective method for loading drugs into MOFs involves the design of functional molecules that serve as construction modules.[20] Biomolecules play a crucial role because of their

[a]*College of Chemistry and Chemical Engineering, Xiamen University, Xiamen, 361005, China*

[b]*College of Energy, Xiamen University, Xiamen, 361102, China*

[c]*Innovation Laboratory for Sciences and Technologies of Energy Materials of Fujian Province (IKKEM), Xiamen, 361005, China. E-mail: sli@xmu.edu.cn*

† Electronic supplementary information (ESI) available: Experimental details and physico-chemical properties of MIL-101 nanoparticles. See DOI: https://doi.org/10.1039/d4ra09107h

unique chemical properties and various active chemical groups that are capable of coordinating with inorganic metals. For instance, biomolecules, such as amino acids, peptides, nucleobases, and carbohydrates, have been extensively utilized as organic ligands to synthesize bioMOFs.[21] These bioMOFs have not only exhibited excellent biocompatibility, they have also been shown to possess specialized biological functions, supporting their significant potential for biomedical applications. However, most bioactive substances are highly flexible and possess low symmetry, posing challenges to the direct formation of high-quality MOF crystals. To address these challenges, researchers must meticulously design and regulate ligands to ensure effective coordination with metal ions and thus form stable and ordered MOF structures.

Acute ischemic stroke is a significant concern in global medical science because of its increasing morbidity, mortality, and disability rates, which pose a serious threat to human life and health.[22] Despite the severity of this disease, effective treatment methods remain scarce and the clinical prevention and therapeutic options endorsed by international experts are limited, which has posed critical challenges to clinical treatment. Thus, investigation into neuroprotective agents against ischemic stroke is imperative.[23] The primary mechanisms of ischemic stroke injury involve brain ischemia, hypoxia, and reperfusion. During ischemia, calcium overload induces the production of mitochondrial reactive oxygen species (ROS) and the activation of calpain. During reperfusion, oxygen contributes to increase intracellular calcium levels, and the continuous generation of ROS leads to the oxidation of phospholipids and proteins, which induces plasma and mitochondrial membrane damage, DNA damage, and cell death.[24,25]

Reducing ischemia/reperfusion (IR)-induced nervous system injury in patients who have suffered a stroke is of paramount clinical significance. Current strategies are focused on reducing intracellular calcium levels and ROS production, inhibiting inflammatory responses, and promoting cell survival.[26,27] Excessive ROS levels can lead to oxidative stress, mitochondrial dysfunction, and cell death. The effects of neuroprotective agents, particularly, antioxidants, on tissues and organs affected by IR have been shown to be promising.[28] However, despite extensive research and identification of numerous neuroprotective compounds, clinical outcomes remain unsatisfactory.[24] The primary challenge in stroke treatment is crossing the blood–brain barrier (BBB).[29,30] The effective delivery of active components to IR-damaged tissues while minimizing non-target toxicity is crucial for the development of neuroprotective agents.[31] Considering this, numerous nano-drug delivery systems have been developed, yielding remarkable results on efforts to minimize IR damage.[29] These nanoparticles (NPs) can carry various payloads, such as small molecules, peptides, antibodies, and nucleic acids, that can contribute to enhance their half-life and bioavailability. Current NPs employed for IR damage treatment include biodegradable NPs (PLGA[32] and chitosan NPs[33]), polymer micelles,[34,35] and inorganic carbon nanotubes.[36] Although significant progress has been made in immobilizing neuroprotective agents using nanotechnology, environmentally friendly large-scale preparation of nano-drug-loaded materials with controlled size, morphology and purity remains challenging. Research is necessary to address these challenges in future clinical trials.

2,2-Dimethylthiazolidine hydrochloride (DMTD), a tetrahydrobenzoic compound, hydrolyzes into cysteine as it mitigates most of its toxicity by masking amino and sulfhydryl groups.[37,38] DMTD can suppresses ROS generation and prevent DNA damage induced by ROS.[37] MIL-101, characterized by low toxicity, a high loading capacity, and good stability, has been reported as excellent drug delivery platform. And research showed that primary human endothelial cells were not affected by MIL-101(Cr) and their derivatives up to high doses of 200 μg mL^{-1} toward with regard to apoptotic cell death or inflammatory responses.[39] Polyethylene glycol (PEG) groups can shield MOFs, facilitating their crossing of the BBB and enhancing cellular uptake *in vitro* and *in vivo*.[40] Thus, in this work, the PEGylation of MOF NPs with dual ligands that have the DMTD structure was synthesized and its potential in mitigating nervous system injury induced by IR during a stroke was investigated (Fig. 1). This novel fabrication strategy extends beyond conventional physical or lowdown modifications to achieve functional modifications of MOF stereo structures more in-depth. Furthermore, we constructed a green ultra-sound-assisted continuous-flow system to efficiently produce MOF nanoparticles sustainably.

Experimental

Materials

Comprehensive material details are provided as ESI.† All animal experiments were approved by the Institutional Animal Care and Use Committee and were in strict accordance with good veterinary practice as defined by the Xiamen University Laboratory Animal Center.

Preparation of MIL-101(Cr)-DM

In a 30 mL autoclave, $Cr(NO_3)_3 \cdot 9(H_2O)$ (0.4 g, 1.0 mmol), 2-(2,2-dimethylthiazolidine-3-carbonyl) terephthalic acid (0.15 g, 0.5 mmol), terephthalic acid (0.17 g, 1.0 mmol), and dimethylformamide (30 mL) were combined and sonicated for 15 min to dissolve the reactants. The solution was then heated to 160 °C and stirred with a magnetic agitator for 15 h. After the reaction, the solution was cooled to room temperature, centrifuged at 800 rpm for 20 min, and the supernatant was banished. The resulting solid was cleaned with 10 mL of distilled water and centrifuged at 800 rpm for 30 min, after which the

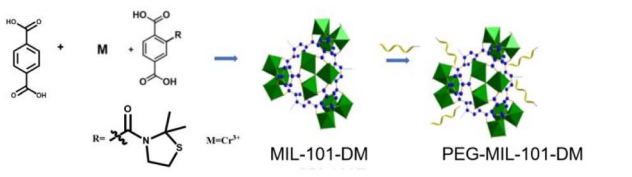

Fig. 1 Fabrication of metal–organic framework based neuroprotection system.

supernatant was discarded. This solid was then washed with 10 mL of acetone, stirred, and centrifuged at 3000 rpm for 30 min, after which the supernatant was discarded. Subsequently, the solid was added to 20 mL of dimethylformamide, stirred at room temperature for 30 min, and centrifuged at 800 rpm for 30 min, after which the supernatant was discarded. Lastly, the solid was mixed with 10 mL of methanol, centrifuged at 800 rpm for 30 min before discarding the supernatant, and vacuum-dried to yield 0.22 g of a brown solid, designated as MIL-101-DM.

Modification of MIL-101(Cr)-DM with PEG

A round-bottomed flask was charged with the previously prepared MIL-101-DM (0.20 g) and dichloromethane (40 mL). The mixture was sonicated for 10 min, followed by three nitrogen purges. PEG2000 (200 mg) was added to the reaction mixture. The solution was stirred at room temperature for 24 h, and the supernatant was removed by subjecting the solution to centrifugation at 800 rpm for 30 min. The resulting solid was sequentially and separately washed with 10 mL of dichloromethane and 10 mL of methanol. Lastly, the brown solid obtained (0.23 g) was vacuum-dried and designated as PEG-MIL-101-DM.

Preparation of MOFs with flow chemistry

The schematic diagram for continuous preparation of MOFs is illustrated in Fig. 2. Solutions of cchromium nitrate (0.06 mol L^{-1}, reservoir 1), terephthalic acid (0.06 mol L^{-1}, reservoir 2), and 2-(2-dimethylthiazolidine-3-carbonyl) terephthalic acid (0.03 mol L^{-1}, reservoir 2) were pumped with HPLC pumps and combined in a Y-type mixer. The mixture was then pumped to a linear reactor (inner diameter: 1/8 inch, length: 100 mm), heated in an oil bath, and placed in an ultrasound (US) generator (40 kHz, 1000 W). The flow rate of each stream was 1.5 mL min^{-1}, resulting in a total flow rate of 3 mL min^{-1}. The system operated at a pressure of 100 psi, with 150 °C. The downstream product was cooled by using a heat exchanger, collected, and filtered to obtain MIL-101UF-DM. The post-processing steps were identical to those used in the batch method to obtain PEG-MIL-101UF-DM.

Cellular uptake and BBB crossing

Five milligrams of MOF NPs (MIL101-DM and MIL101-DM-PEG) were combined with 0.5 mg of rhodamine B isothiocyanate (RITC) in 10 mL of H_2O and binded for 6 h. Following centrifugation, the RITC-binded MOF NPs were dispersed in Dulbecco's Modified Eagle's Medium (DMEM) at a concentration of 100 ppm. The primary brain capillary endothelial cells (BCECs) were isolated as follows: rat brain tissues were digested with collagenase II and DNase I, followed by Percoll gradient centrifugation to isolate microvessel fragments. A secondary digestion was then performed to obtain single cells. The cells were cultured in DMEM/F12 medium supplemented with 20% FBS and ECGS. Primary brain capillary endothelial cells were seeded into 6-well microplates at a density of 105 cells per well and allowed to adhere overnight at 37 °C under 5% CO_2. The culture medium was then replaced with DMEM containing MOFs NPs. Following co-incubation for 1, 4, or 8 h, the BCECs were rinsed three times with phosphate-buffered saline (PBS) to remove non-uptake MOF NPs and subsequently analyzed by applying flow cytometry using R-phycoerythrin. Concurrently, BCECs were seeded into a CLSM-specific cell culture dish, treated as described above, and stained with DAPI. The cellular uptake of MOF NPs was detected by applying confocal fluorescence using an Olympus FV1000 laser-scanning microscope with excitation at 358 nm for DAPI (4′,6-diamidino-2-phenylindole) and 540 nm for RITC.

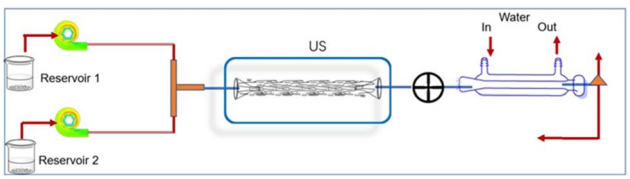

Fig. 2 Preparation of MIL-101UF-DM with flow chemistry.

Oxygen and glucose deprivation and H_2O_2 model

The pathological model of IR injury was simulated by applying oxygen and glucose deprivation (OGD) and reoxygenation. To induce OGD, SH-SY5Y cells were cultured in glucose-free DMEM containing 2 mM $Na_2S_2O_4$ at 37 °C for 1 h. Subsequently, SH-SY5Y cells were recovered to normal conditions and re-oxygenated for another twenty-four hours, with the MOFs (5 μM) added at the start of re-oxygenation. An H_2O_2 cell model was utilized to mimic ischemia-induced oxidative stress. Briefly, SH-SY5Y cells were cultured with the MOFs (5 μM) for one hour, after which an H_2O_2 solution was added to the medium at concentrations of 500 μM. The cells were inoculated for either three hours or one day. The SH-SY5Y cell line was purchased from Shanghai Enzyme Research Biotechnology Co., Ltd.

Cell viability evaluation

Cell viability was assessed by using an MTT assay (abcam). For the cytotoxicity evaluation, SH-SY5Y cells were seeded in 96-well plates (1×10^4 cells per well), incubated for 24 h, and then cultured with various concentrations of the MOFs for 24 h. The cells were subsequently evaluated with the MTT assay and detected at 490 nm.

For the OGD experiment, SH-SY5Y cells were inoculated in 96-well plates and treated as previously described. Following 24 h of re-oxygenation, cell viability was evaluated by applying an MTT assay. For the H_2O_2 experiment, SH-SY5Y cells were seeded in 96-well plates, cultured overnight, and treated with the MOFs. After one hour, the cells were exposed to a 500 μM H_2O_2 solution for three hours, and cell viability was measured by applying an MTT assay.

Intracellular ROS levels detection

SH-SY5Y cells were seeded in 6-well plates (4×10^5 cells per well) and cultured overnight. After being subjected to OGD for

one hour, the cells were re-oxygenated for twenty-four hours, with the MOF NPs admission before the re-oxygenation process. The cells were then collected and cultured with 2′,7′-dichlorodihydrofluorescein diacetate (DCFH-DA) at a concentration of 5 μM for 30 min at 37 °C. The value of ROS in SH-SY5Y cells were evaluated by measuring the mean fluorescence intensity of DCFH-DA with flow cytometry.

Statistical analysis

Mean comparisons were achieved by conducting unpaired two-tailed *t*-tests with GraphPad Prism 5. Data are presented as the mean ± standard deviation of the mean, with differences considered statistically significant at $p < 0.05$.

Results and discussion

Fabrication of MOF nanoparticles

To address the limitations of the adsorption and chemical grafting methods, we utilized functional molecules as ligands to construct the MOF structure (Fig. 1). Initially, MIL-101-DM was synthesized *via* a hydrothermal method in which the ratio of terephthalic acid (ligand 1) to 2-(2-dimethylthiazolidine-3-carbonyl) terephthalic acid (ligand 2) was meticulously adjusted. A high proportion of ligand 2 negatively affected the overall crystal properties of the MOF materials, whereas an excess of ligand 1 reduced the presence of active functional components. Following optimization, a ligand 1-to-ligand 2 ratio of 2 : 1 was selected to construct the MIL-101-DM. Following synthesis of the MOF nanocrystals, PEG was adsorbed onto the surface of the MOF material.

The prepared MOFs are characterized by scanning electron microscopy (SEM) (Fig. 3A). The nanocrystals exhibited a rod shape and had unified particle sizes (diameter: ~250–350 nm). The porosities of MIL-101-DM and MIL-101-DM-PEG were measured by conducting N_2 adsorption experiments (Table S2†). The BET surface areas of MIL-101-DM and PEG-MIL-101-DM were 839 and 435 $m^2\ g^{-1}$, respectively. The crystallinity of MIL-101-DM and PEG-MIL-101-DM was detected *via* X-ray powder diffraction (PXRD) (Fig. 3B). These characteristic peaks were consistent with those of the simulated MIL-101, confirming their crystal structures.[41,42]

After adsorption with PEG fragment, a peak was found at 2880 cm^{-1} in the Fourier-transform infrared (FTIR) spectra, which belongs to hydroxyl group (Fig. S6†).[43] The Fourier transform infrared spectroscopy strong bands at 1300–1800 cm^{-1} belong to ν_{as}(COO), ν_s(COO), and ν(C–C) stretching vibrations from the dicarboxylate linker in the MIL-101 framework (Table S1†). The thermal stabilities of MIL-101-DM and PEG-MIL-101-DM were measured by thermogravimetric analysis (TGA) (Fig. S7†). The analysis revealed two distinct weight-loss processes. The first occurred between 25 and 360 °C, corresponding to the disappearance of the MeOH solvent and PEG fragment, and it accounted for approximately 16 wt% of the weight loss. The subsequent weight loss of about 47% has been attributed to matrix collapse of the MOF.

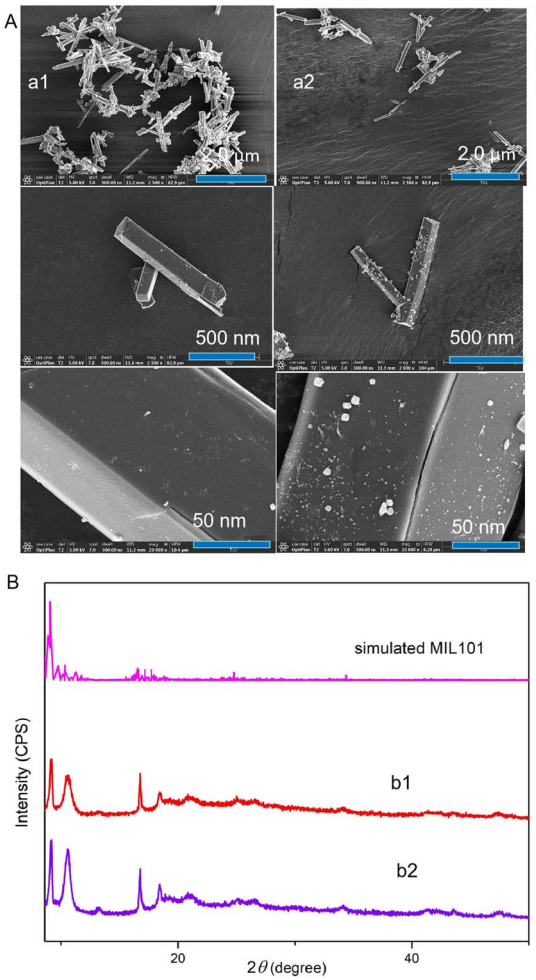

Fig. 3 (a) SEM images of the prepared MOFs: (a1) MIL-101-DM and (a2) PEG-MIL-101-DM. (b) PXRD spectra of (b1) MIL-101-DM and (b2) PEG-MIL-101-DM.

The stability of PEG-functionalized MOFs in various solutions was assessed by transferring the NPs to water, PBS, and simulated intestinal fluid (SIF). Surface PEGylation significantly enhanced the stability of the synthesized MOFs. The release of Cr^{3+} from MIL-101-DM exceeded 70%, whereas it was only approximately 40% for PEG-MIL-101-DM (Fig. 4A). The experimental results indicate that PEGylation enhanced the stability of the MOFs in the SIF. The collapses of MOF were measured with Cr^{3+} ions after a specified time (Fig. 4B) in PBS. Particularly, about 35% of Cr^{3+} was released from PEG-MIL-101-DM, whereas 75% was released from MIL-101-DM. The PEGylated MOFs nanoparticles had a size of 370 nm in methanol solution (0.4 mg mL^{-1}), as measured by dynamic light scattering (DLS) (Fig. S8†).

Continuous preparation of MIL-101-DM nanoparticles

Flow chemistry offers a green and efficient strategy for the synthesis of MOFs with more green strategy.[44,45] For our work, MIL-101-DM was fabricated by ultrasound assisted flow chemistry tactics (Fig. 2). This method has been increasingly reported

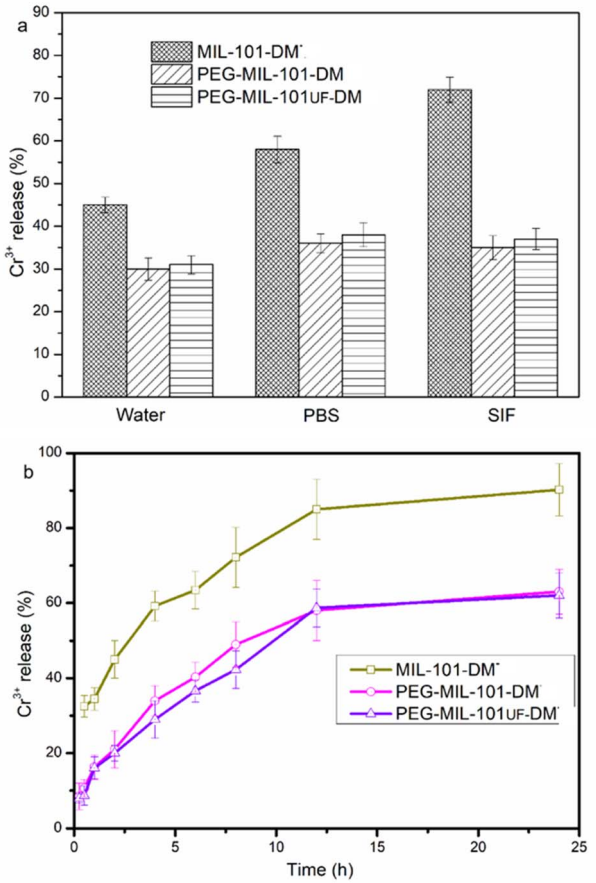

Fig. 4 (a) MIL-101-DM and PEG-MIL-101-DM in water, PBS, and SIF over a period of 4 h at 37 °C. (b) MIL-101-DM and PEG-MIL-101-DM in PBS at 37 °C.

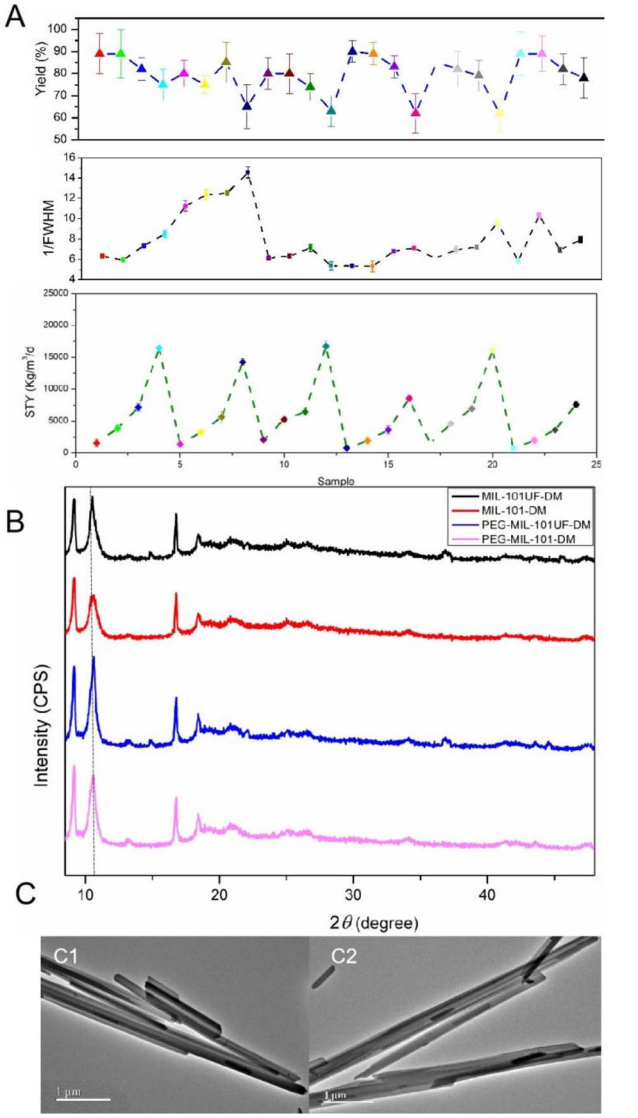

Fig. 5 (A) Graphical summary of the yield, space-time yield (STY), and crystallinity (1/[full width at half-maximum (FWHM)]) for each experiment conducted with ultrasound-assisted multistep continuous-flow synthesis (n = 3, mean values). (B) X-ray diffraction spectra of MOFs NPs under batch and flow conditions. (C) Transmission electron microscopy (TEM) analysis of (c1) PEG-MIL-101-DM and (c2) PEG-MIL-101UF-DM.

to produce MOFs with a high space-time yield (STY) and excellent quality. The ultrasound rig in flow chemistry can generate a lot of bubbles, which is acoustic cavitation.[46] This results in intense internal heating and high pressure inside of the reactor over short periods of time. The metal ions, ligand 1, and ligand 2 were dissolved in DMF, combined in a Y-type mixer, and transferred into the reactive channel equipped with ultrasound rig. The impacts of reactive conditions, including the flow rate (1.0, 2.0, and 5.0 mL min^{-1}), temperature (130, 150, and 170 °C), reactant concentration (0.03, 0.06, and 0.12 mol L^{-1}), and applied ultrasound, on the STY, yield, and crystallinity of MOF NPs (Fig. 5A and Table S3†). The full width at half-maximum (FWHM) of the relevant PXRD peaks was studied to characterized the quality of synthesized MOFs. By optimizing these key reaction parameters, we were able to synthesize MOF NPs, without compromising product quality, by using the continuous-flow method. Ultrasound enhanced MOF fabrication efficacy by concentrating the sound energy in the reaction mixture, with acoustic cavitation generating intense internal heating and high pressure inside of the reactor.[47]

The response surface method (RSM) has been used extensively to optimize reaction processes and achieve optimal conditions.[48] To enhance the synthesized MIL-101UF-DM, a series of experiments were conducted by employing a Box–Behnken design (BBD) to optimize the experimental conditions (details provided as ESM†). A quadratic model was employed and its probability value was less than 0.0001, and it had the lowest standard deviation. Values for the Fisher's test, probability, lack-of-fit F-value, coefficient of variation, and adequate precision were calculated by using ANOVA. The final equation in terms of the coded factors is as follows:

$$\frac{1}{\mathrm{FWHM}} = 8.67 - 0.49A - 0.36B + 0.49C - 0.22AB - 0.41AC + 0.18BC - 1.48A^2 + 0.032B^2 - 2.11C^2 \quad (1)$$

where *A*, *B*, and *C* denote the flow rate, chromic ion, and rig temperature, respectively. Three-dimensional response surface plots were generated by employing the proposed quadratic regression model from eqn (1) to explore the impacts. These plots illustrate that increasing the flow rate and concentration resulted in poor crystallinity (indicated by a low 1/FWHM), whereas a low flow rate and low concentration led to a low STY. Notably, intermediate temperatures were found to be conducive to the synthesis of high-quality MOF synthesis.

Based on these findings, the continuous flow reaction was conducted under the conditions of 150 °C and 60 psi in a 3 mL reactor coil with a flow rate of 2.0 mL min^{-1}, resulting in a residence time of 1.5 min. Under these conditions, a yield of 80% and STY of 5664 kg m^{-3} d^{-1} were achieved. Additionally, the classical batch method typically produces MOFs on a milligram scale over several days. However, our method achieved a high STY, which significantly reduced the energy and resources required for large-scale MOF fabrication. The downstream product was cooled and filtered to obtain MIL-101UF-DM. They were PEGlated in the same way and used for biological assays.

The PXRD pattern of MIL-101UF-DM exhibits similar characteristic peaks with that of MIL-101-DM (Fig. 5B), demonstrating that few impurities were produced by the continuous method. TEM analyses showed that the particles prepared by the flow reactor setup exhibited diameters of 250–350 nm (Fig. 5c2), which are consistent with the NPs produced using the batch method (Fig. 5c1). MIL-101UF-DM exhibited BET surface areas over 800 m^2 g^{-1} (Table S4†). The MOF materials synthesized *via* both methods exhibit comparable physicochemical properties. The flow-synthesized MIL-101UF-DM and PEG-MIL-101UF-DM were used for biological assays. S content in surface layer of MIL-101UF-DM measured by XPS (X-ray photoelectron spectroscopy) is 2.24 atomic%. The peak of binding energy at around 163.8 eV indicated the oxidation state of S and the presence of C–S–C bond (Fig. S4†). The sulfur content of MIL-101UF-DM detected by elemental analysis (C, H, N, S, Table S2†) is 4.66% (wt%). This demonstrates that the incorporation degree is not linearly proportional to the initial molar ratios. After PEG modification, the sulfur content in PEG-MIL-101UF-DM was measured to be 4.21% (wt%), which corresponds to approximately 40 wt% of ligand 2 in the composite material.

Neuroprotective ability of PEG-MIL-101UF-DM on SH-SY5Y cells

Initially, we explored the toxicity of MIL-101UF-DM and PEG-MIL-101UF-DM on SH-SY5Y cells. Both MOFs exhibited no toxicity for SH-SY5Y cells when the concentrations were below 5 μM (Fig. 6A). Therefore, a concentration of 5 μM was selected to evaluate their neuroprotective ability. In this work, OGD and H_2O_2 were employed to establish in *in vitro* ischemic stroke models.[49] As shown in Fig. 6B and C, the survival rate of SH-SY5Y cells significantly decreased after OGD or H_2O_2 stimulation ($p < 0.001$). The cell survival rates of treatment groups became higher relative to those exposed to OGD or H_2O_2 alone. Additionally, cells treated with PEG-MIL-101UF-DM exhibited higher survival rates than those treated with MIL-101UF-DM in both the OGD and H_2O_2 models ($p < 0.05$), showing that PEG-MIL-101UF-DM yielded neuroprotective effects.

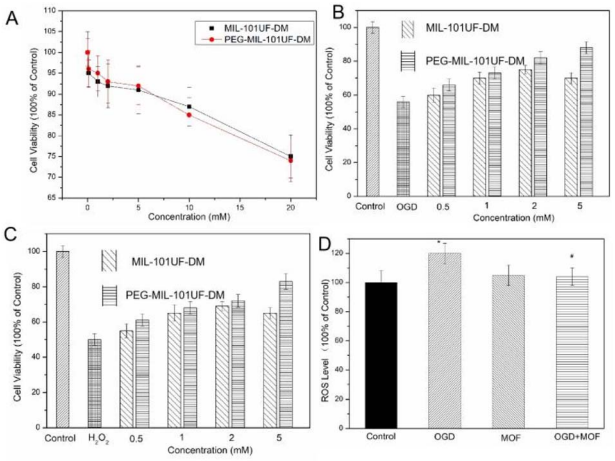

Fig. 6 Neuroprotective effects. (A) Toxicity of MIL-101UF-DM and PEG-MIL-101UF-DM for SH-SY5Y cells. (B) and (C) The survival rate of SH-SY5Y cells significantly decreased after OGD or H_2O_2 stimulation. (D) Oxidative stress in SH-SY5Y cells.

PEG-MIL-101UF-DM-improved oxidative stress in SH-SY5Y cells

As shown in Fig. 6D, ROS levels were significantly higher in the OGD group than in the control group ($p < 0.05$). However, the ROS levels in the OGD + MOF group were markedly lower than those in the OGD group ($p < 0.01$). These data suggested that PEG-MIL-101UF-DM prevented ROS accumulation in SH-SY5Y cells, potentially accounting for its cytoprotective effects against oxidative stress.

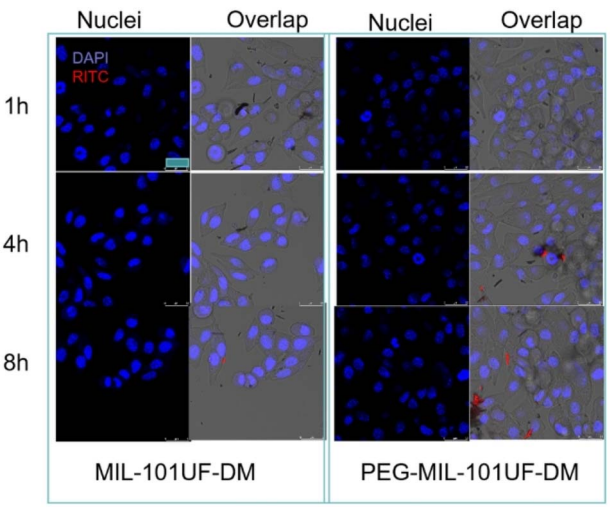

Fig. 7 Confocal laser-scanning microscopy images of BCECs incubated with MIL-101UF-DM and PEG-MIL-101UF-DM for 1, 4, and 8 h at a concentration of 50 ppm of ceria NPs. Scale bars represent 20 μm. Blue: the nuclei of BCECs stained with DAPI. Red: MIL-101 nanoparticles labeled with RITC.

PEG-MIL-101UF-DM-improved cellular uptake and BBB crossing *in vitro*

BCECs co-cultured with the aforementioned NPs was characterized by confocal microscopic (Fig. 7). A strong red fluorescence signal of RITC was found to surround the nuclei of the BCECs treated with PEG-MIL-101UF-DM, whereas a much weaker fluorescence signal was detected for MIL-101UF-DM under the same conditions. These results clearly confirm the significantly higher cellular uptake of PEG-MIL-101UF-DM compared to that of MIL-101UF-DM by BCECs, in terms of both quantity and rate. This enhanced uptake could be attributed to the ability of PEG-MIL-101UF-DM to cross the BBB.[50] Additionally, PEG-MIL-101UF-DM exhibited significant uptake after incubation for 4 h, and its uptake further increased after 8 h, indicating that the particles possess good stability, so that have capacity of protecting the BCECs against oxidation-induced death in the BBB.

Conclusions

The development of a controllable drug delivery system is essential for minimizing side effects and enhancing drug efficacy. In this study, MIL-101-DM nanoparticles were prepared with two kinds of ligands (terephthalic acid, and 2-(2-dimethylthiazolidine-3-carbonyl) terephthalic acid). Furthermore, PEG2000 was encapsulated in the MOFs to cross BBB. We constructed a green ultrasound-assisted continuous-flow system to efficiently produce MOF nanoparticles with a high STY and good quality. The MOF behaved protective activity in SH-SY5Y cells against oxygen and glucose deprivation and H_2O_2 insults, and prevent reactive oxygen species accumulation. Therefore, the PEGylated MOF nanoparticles have the potential to be used as a promising therapeutic candidate to reduce ischemia/reperfusion-induced nervous system injury.

Data availability

The authors declare that the data supporting the findings of this study are available in the article. The data supporting this article have also been included as part of the ESI.† Any relevant datasets are properly cited in the reference section.

Author contributions

Conceptualization, S. L.; methodology, Y.·W.; formal analysis, Y.·W.; investigation, data curation, Y.·W.; writing – original draft preparation, Y.·W.; writing – review and editing, S. L.; visualization, S. L.; supervision, S. L.; project administration, S. L.; funding acquisition, S. L. All authors have read and agreed to the published version of the manuscript.

Conflicts of interest

There are no conflicts to declare.

Acknowledgements

This research was funded by Natural Science Foundation of Xiamen, China (File no. 2022CXY0116). The acknowledgements come at the end of an article after the conclusions and before the notes and references.

Notes and references

1 Z. S. Sayed, E. M. Hieba, H. A. Batakoushy, H. R. M. Rashdan, E. Ismail, S. M. Elkatlawy and A. Elzwawy, *RSC Adv.*, 2024, **14**, 39297–39324.
2 Q. Q. Huang, Y. K. Chen, W. W. Zhang, X. Xia, H. M. Li, M. Qin and H. L. Gao, *J. Control. Release*, 2024, **366**, 519–534.
3 P. Ma, X. Lai, Z. Luo, Y. Chen, X. J. Loh, E. Ye, Z. Li, C. Wu and Y.-L. Wu, *Nanoscale Adv.*, 2022, **4**, 3462–3478.
4 D. S. R. Khafaga, M. T. El-Morsy, H. Faried, A. H. Diab, S. Shehab, A. M. Saleh and G. A. M. Ali, *RSC Adv.*, 2024, **14**, 30201–30229.
5 W. J. Li, Z. Q. Wang, J. B. Wang, R. Wu, H. W. Shi, E. X. Liu, M. Zhang and Z. H. Zhang, *J. Catal.*, 2024, **430**, 115308.
6 S. Mallakpour, E. Nikkhoo and C. M. Hussain, *Coord. Chem. Rev.*, 2022, **451**, 214262.
7 X. Zhao, Y. Wang, X. Gao, X. Gao, M. Wang, H. Huang and B. Liu, *Chin. Chem. Lett.*, 2025, **36**, 109901.
8 S. L. Kang, T. Yue, D. D. Su, W. J. Shi, P. C. Jiang and Z. H. Zhang, *ACS Sustainable Chem. Eng.*, 2024, **12**, 124.
9 Y. Guo, Y. T. Li, S. J. Zhou, Q. S. Ye, X. J. Zan and Y. He, *ACS Biomater. Sci. Eng.*, 2022, **8**, 4028–4038.
10 Y. T. Li, K. Zhang, P. R. Liu, M. Chen, Y. L. Zhong, Q. S. Ye, M. Q. Wei, H. J. Zhao and Z. Y. Tang, *Adv. Mater.*, 2019, **31**, 1901570.
11 T. C. Livesey, L. A. M. Mahmoud, M. G. Katsikogianni and S. Nayak, *Pharmaceutics*, 2023, **15**(1), 274.
12 P. G. M. Mileo, D. N. Gomes, D. V. Gonçalves and S. M. P. Lucena, *Adsorption*, 2021, **27**, 1123–1135.
13 N. Motakef-Kazemi, S. A. Shojaosadati and A. Morsali, *Microporous Mesoporous Mater.*, 2014, **186**, 73–79.
14 M. Mojtaba, A. Ehsani, M. Shahi, S. Gharanli, H. Saremi, R. E. Malekshah, Z. S. Basmenj, S. Salmani and M. Mohammadi, *J. Drug. Delivery Sci. Tecnol.*, 2023, **81**, 104285.
15 J. Y. Oh, E. Choi, B. Jana, E. M. Go, E. J. Jin, S. Jin, J. Lee, J. H. Bae, G. S. Yang, S. K. Kwak, W. Y. Choe and J. H. Ryu, *Small*, 2023, **19**, 2300218.
16 S. Peng, B. L. Bie, Y. Z. S. Sun, M. Liu, H. J. Cong, W. T. Zhou, Y. C. Xia, H. Tang, H. X. Deng and X. Zhou, *Nat. Commun.*, 2018, **9**, 1293.
17 S. Saad, M. T. Marcos-Almaraz, N. Menguy, J. Scola, J. Volatron, R. Rouland, J. M. Grenèche, S. Miraux, C. Menet, N. Guillou, F. Gazeau, C. Serre, P. Horcajada and N. Steunou, *Chem*, 2017, **3**, 303–322.
18 B. L. Tao, W. K. Zhao, C. C. Lin, Z. Yuan, Y. He, L. Lu, M. W. Chen, Y. Ding, Y. L. Yang, Z. Z. L. Xia and K. Y. Cai, *Chem. Eng. J.*, 2020, **390**, 124621.
19 M. X. Wu and Y. W. Yang, *Adv. Mater.*, 2017, **29**, 1606134.

20 H. D. Lawson, S. P. Walton and C. Chan, *ACS Appl. Mater. Interfaces*, 2021, **13**, 7004–7020.
21 H. D. An, M. M. Li, J. Ga, Z. J. Zhang, S. Q. Ma and Y. Chen, *Coord. Chem. Rev.*, 2019, **384**, 90–106.
22 J. G. Hankey, *Lancet*, 2017, **389**, 641–654.
23 Y. Béjot, *J. Neurol.*, 2021, **268**, 785–795.
24 K. H. Eltzschig and T. Eckle, *Nat. Med.*, 2011, **17**, 1391–1401.
25 W. Zhang, T. Tian, S. X. Gong, W. Q. Huang, Q. Y. Zhou, A. P. Wang and Y. Tian, *Neural Regener. Res.*, 2021, **16**, 6–11.
26 M. Y. Wu, G. T. Yiang, W. T. Liao, A. P. Y. Tsai, Y. L. Cheng, P. W. Cheng, C. Y. Li and C. J. Li, *Cell. Physiol. Biochem.*, 2018, **46**, 1650–1667.
27 R. O. S. Soares, D. M. Losada, M. C. Jordani, P. Évora and O. Castro-e-Silva, *Int. J. Mol. Sci.*, 2019, **20**(20), 5034.
28 T. J. Zhao, W. Wu, L. H. Sui, Q. Huang, Y. Y. Nan, J. H. Liu and K. L. Ai, *Bioact. Mater.*, 2022, **7**, 47–72.
29 S. Majid, M. Eslamifar, K. Khezri and S. M. Dizaj, *Biomed. Pharmacother.*, 2019, **111**, 666–675.
30 A. D'Souza, K. M. Dave, R. A. Stetler and D. S. Manickam, *Adv. Drug Delivery Rev.*, 2021, **171**, 332–351.
31 X. Y. Jiang, A. V. Andjelkovic, L. Zhu, T. Yang, M. Bennett, J. Chen, R. F. Keep and Y. J. Shi, *Prog. Neurobiol.*, 2018, **163**, 144–171.
32 S. Pushkar, T. Arsiwala and W. J. Geldenhuys, *Int. J. Pharmaceut.*, 2020, **578**, 119090.
33 S. K. Verma, I. Arora, K. Javed, M. Akhtar and M. Samim, *ACS Appl. Mater. Interfaces*, 2016, **8**, 19716–19723.
34 Y. Wang, S. Y. Li, S. Shen and J. Wang, *Biomaterials*, 2018, **161**, 95–105.
35 C. Zhang, C. L. Ling, L. Pang, Q. Wang, J. X. Liu, B. S. Wang, J. M. Liang, Y. Z. Guo, J. Qin and J. X. Wang, *Theranostics*, 2017, **7**, 3260–3275.
36 H. R. Fabian, P. J. Derry, H. C. Rea, W. V. Dalmeida, L. G. Nilewski, W. K. A. Sikkema, P. Mandava, A. L. Tsai, K. Mendoza, V. Berka, J. M. Tour and T. A. Kent, *Front. Neurol.*, 2018, **9**, 199.
37 D. Bo, Q. Y. Su, X. Liu, X. Mi, L. Dou, D. H. Zhou, Y. Su, T. Y. Shen, Y. Y. Zhang, W. Q. Xu, X. Y. Tan and D. K. Wang, *Biochem. Biophs. Res. Commun.*, 2023, **679**, 15–22.
38 M. Tsutomu, Y. Kohama, S. Kuwahara, K. Yamamoto, Y. Komiyama, M. Satake, Y. Chiba, K. Miyashita, T. Tanaka, T. Imanishi and C. Iwata, *Chem. Pharm. Bull.*, 1988, **36**, 1110–1116.
39 S. Wuttke, A. Zimpel, T. Bein, S. Braig, K. Stoiber, A. Vollmar, D. Müller, K. Haastert-Talini, J. Schaeske, M. Stiesch, G. Zahn, A. Mohmeyer, P. BehrensE, O. Eickelberg, D. A. Bölükbas and S. Meiners, *Adv. Healthcare Mater.*, 2017, **6**, 1600818.
40 E. C. M. de Lange and M. Hammarlund-Udenaes, *Clin. Pharmacol. Ther.*, 2015, **97**, 380–394.
41 G. Férey, C. Mellot-Draznieks, C. Serre, F. Millange, J. Dutour, S. Surblé and I. Margiolaki, *Science*, 2005, **309**, 2040–2042.
42 O. I. Lebedev, F. Millange, C. Serre, G. Van Tendeloo and G. Férey, *Chem. Mater.*, 2005, **17**, 6525–6527.
43 I. A. Lazaro, S. Haddad, S. Sacca, C. Orellana-Tavra, D. Fairen-Jimenez and R. S. Forgan, *Chem*, 2017, **2**, 561–578.
44 M. Rubio-Martinez, C. Avci-Camur, A. W. Thornton, I. Imaz, D. Maspoch and M. R. Hill, *Chem. Soc. Rev.*, 2017, **46**, 3453–3480.
45 D. S. Raja and D. H. Tsai, *Chem. Commun.*, 2024, **60**, 8497–8515.
46 Z. Q. Li, L. G. Qiu, T. Xu, Y. Wu, W. Wang, Z. Y. Wu and X. Jiang, *Mater. Lett.*, 2009, **63**, 78–80.
47 N. S. M. Yusof, S. Anandan, P. Sivashanmugam, E. M. M. Flores and M. Ashokkumar, *Ultrason. Sonochem.*, 2022, **85**, 105988.
48 J. Guo, Y. K. Zhang, W. Zhang, Y. Miao, T. T. Lu and J. Xia, *Fresenius Environ. Bull.*, 2019, **28**, 4891–4895.
49 X. N. Xu, Z. M. Wu, H. Y. Qiu and J. Wu, *Neuropsychiatr. Dis. Treat.*, 2020, **17**, 147–156.
50 Q. Q. Bao, P. Hu, Y. Y. Xu, T. S. Cheng, C. Y. Wei, L. M. Pan and J. L. Shi, *ACS Nano*, 2018, **12**, 6794–6805.